Inorganic Chemistry

Article

pubs.acs.org/IC

Dimensional and Coordination Number Reductions in a Large Family of Lanthanide Tellurite Sulfates

Jian Lin,[†] Kariem Diefenbach,[†] Naoki Kikugawa,[‡,§] Ryan E. Baumbach,[‡] and Thomas E. Albrecht-Schmitt*[,†]

[†]Department of Chemistry and Biochemistry, Florida State University, 95 Chieftan Way, Tallahassee, Florida 32306, United States

[‡]National High Magnetic Field Laboratory, 1800 E. Paul Dirac Drive, Tallahassee, Florida 32310, United States

[§]National Institute for Materials Science, 1-2-1 Sengen, Tsukuba, Ibaraki 305-0044, Japan

Supporting Information

ABSTRACT: Twenty-two new lanthanide tellurite sulfates with five distinct structures, $Ln_2(Te_2O_5)(SO_4)_2$ (Ln = La, Ce, Pr, Nd, Sm, Eu, Gd, Tb; **LnTeSO-1**), $Ho_3(TeO_3)_2(SO_4)_2(OH)(H_2O)$ (**LnTeSO-2**), $Ln_2TeO_3(SO_4)_2(H_2O)_2$ (Ln = Dy, Ho, Er; **LnTeSO-3**), $Ln_2(Te_2O_5)(SO_4)_2$ (Ln = Er, Tm, Yb, Lu; **LnTeSO-4**), and $Ln_2(Te_4O_{10})(SO_4)$ (Ln = Gd, Dy, Ho, Er, Tm, Yb; **LnTeSO-5**), have been prepared and characterized. The topologies of **LnTeSO-1**, **LnTeSO-2**, **LnTeSO-3**, **LnTeSO-4**, and **LnTeSO-5** are substantially different with respect to the connectivity between Ln polyhedra and the coordination environments of the lanthanide ions. For the first four topologies, the dimensionality changes from layered (**LnTeSO-1**) to chains (**LnTeSO-2**) to tetramers (**LnTeSO-3**) and finally to a monomer (**LnTeSO-4**). The coordination numbers of lanthanides decrease from nine (**LnTeSO-1**) to eight (**LnTeSO-2** and **LnTeSO-3**) to seven and six (**LnTeSO-4**). We attribute the transitions to a decrease in the ionic radii of the 4f ions. Magnetic susceptibility measurements reveal no evidence for long-range magnetic ordering in these materials. However, diverse short-range magnetic correlations were observed within **LnTeSO-1**.

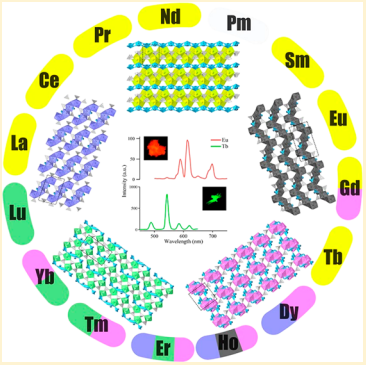

INTRODUCTION

The term lanthanide contraction was originally applied to explain why second- and third-row transition metals are similar in size and is a reference to the poor shielding of nuclear charge by 4f orbitals. Today this term is more generally used to describe the highly systematic reduction in ionic radii that occurs across the 4f series, which is on the order of 0.01 Å between neighboring trivalent ions. A given structure type will have a window of stability for which it can tolerate changes in the size and charge of its constituents without being forced to adopt a different architecture. Some structure types, such as rock salt[1] and glasserite,[2] are remarkably permissive to isovalent and aliovalent substitution, but these become less common as the structural and compositional complexity increases.[3] The regular pattern of decrease in ionic radii by lanthanide ions allows one to observe phase changes induced by very small changes in ion sizes. Many tomes have been written detailing these structural changes since high purity lanthanides became available as a result of the Manhattan Project.[4] The effects of the decreasing ionic radius on the crystal lattice plays an important role in the fine-tuning of the properties of rare-earth materials and can in fact be used to induce pressure effects that dramatically alter magnetic properties.[5]

In addition, the structural chemistry of lanthanides is rich owing to high coordination numbers and a general lack of geometric preferences. Both of these attributes are ascribed to the nearly purely ionic bonding of trivalent lanthanides, and the fact that the 4f orbitals are core-like, and essentially play no role in the arrangement of the surrounding ligands.[6] Coordination numbers of six to 10 are well-represented, with eight- and nine-coordinate lanthanides being the most common. However, environments with as few as three (e.g., $Ln[N(SiMe_3)_2]_3(NCMe)_2$),[7] and as many as 12 (e.g., $[Ce(NO_3)_6]^{2-}$),[8] donor atoms have precedence in the literature. While a relatively isotropic arrangement of ligands is both the norm and expected because the coordination geometry should simply be dictated by repulsion between ligands, highly anisotropic environments, while rare, are also known such as the pentagonal bipyramidal environment found in $[M_2Te_4O_{11}]X_2$ (M = Pu, Ce, Zr; X = Cl, Br; CN = 7), the hula hoop geometry found in $Ln_4[B_{18}O_{25}(OH)_{13}Cl_3]$ (Ln = Sm, Eu; CN = 9), and the capped triangular cupola (CN = 10) environment observed in $Ln[B_4O_6(OH)_2Cl]$ (Ln = La–Nd; Pu).[6,9] These atypical geometries are thought to be enforced by the rigidity of the anionic networks.[6,10]

Lanthanide complexes and materials have been exploited because the lanthanide ions impart large magnetic moments and anisotropy, which when coupled with itinerant magnetism from transitional metals leads to the strongest permanent

Received: May 19, 2014
Published: August 6, 2014

   dx.doi.org/10.1021/ic501163x | Inorg. Chem. 2014, 53, 8555–8564

magnets known, $SmCo_5$ and $Nd_2Fe_{14}B$.[11] Lanthanide magnetism is complex owing to electron repulsion, spin−orbit coupling, and crystal field effects.[12] Spin−orbit coupling is more prominent in lanthanides than in 3d transition metals; thus the orbital angular momentum must be taken into greater consideration for the 4f elements.[13] Furthermore, the ligand field, as well as the geometry of the lanthanide ions, is strongly correlated to the local anisotropy of the lanthanide.[14] The diversity of coordination geometries of lanthanides enables different bonding geometries between metal ions, resulting in a variety of magnetic exchange pathways.[15] Hughes et al.'s study suggests that the change of an atomic unit cell volume, invoked by the lanthanide contraction, plays a distinct role in determining magnetic properties.[16]

The optical properties of lanthanide ions such as luminescence and the Alexandrite effect make this series of materials even more intriguing to work with. Lanthanide luminescence originates in the special features of the electronic transitions of the trivalent Ln^{3+} ions involving a redistribution of electrons within the 4f subshell.[17] Ln^{3+} ions show luminescence in either visible regions (Eu^{3+} and Tb^{3+}) or near-infrared regions (Nd^{3+}, Er^{3+}, and Yb^{3+}).[18] The Eu^{3+}:Y_2O_3 and the Nd^{3+}:YAG lasers are a ubiquitous component of modern technology.[19] Furthermore, some lanthanide containing materials, for example, $Li_5Nd_3Ta_2O_{12}$[20] and $Ho_2Cu(TeO_3)_2(SO_4)_2$,[21] change their color under different lighting conditions, which is referred to as the Alexandrite effect.

While lanthanide intermetallic compounds have played keys roles in the development of magneto-structural correlations, oxoanion systems are also extremely well developed.[22] Tellurium-containing oxoanion compounds are particularly rich for a variety of reasons that include variable coordination numbers, the presence of a stereochemically active lone pair of electrons, and the ability for forming polymeric anionic networks for Te(IV).[23] These compounds, as well as those containing far rarer Te(VI), have been extensively studied by Schleid and co-workers.[24] Concomitant with these developments has been the exploration of mixed oxoanion systems with f-block elements, one example of which is $Ce_2(Te_2O_5)(SO_4)_2$.[9a,23a] The expansion of these studies to encompass the entire lanthanide series is described in this report. Herein, we present the syntheses, structures, and magnetic properties of a large family of lanthanide tellurite sulfates.

EXPERIMENTAL SECTION

Synthesis. La_2O_3, CeO_2, Pr_6O_{11}, Nd_2O_3, Sm_2O_3, Eu_2O_3, Gd_2O_3, Tb_4O_7, Dy_2O_3, Ho_2O_3, Er_2O_3, Tm_2O_3, Yb_2O_3, Lu_2O_3 (99.9%, Alfa-Aesar), TeO_2 (99.99%, Alfa-Aesar), and concentrated H_2SO_4 (98%, Alfa-Aesar) were all used as received. Reactions were run in PTFE-lined Parr 4749 autoclaves with 23 mL internal volume autoclaves. Distilled and Millipore filtered water with a resistance of 18.2 MΩ·cm was used in all reactions.

$Ln_2(Te_2O_5)(SO_4)_2$ (Ln = La, Ce, Pr, Nd, Sm, Eu, Gd, and Tb; LnTeSO-1). Ln_2O_3 (Ln = La, Nd, Sm, Eu, Gd; 0.5 mmol)/CeO_2 (1 mmol, 0.1721 g)/Pr_6O_{11} (0.167 mmol, 0.1702)/Tb_4O_7 (0.25 mmol, 0.1869), TeO_2 (1 mmol, 0.1596 g), 1 M H_2SO_4 (1 mmol, 1 mL), and 1 mL of H_2O were loaded into a 23 mL PTFE-lined autoclave liner. For $Gd_2(Te_2O_5)(SO_4)_2$ synthesis, $CrCl_3$ (0.5 mmol, 0.1332 g) was added with the presence of Gd_2O_3, TeO_2, and H_2SO_4.

$Ho_3(TeO_3)_2(SO_4)_2(OH)(H_2O)$ (LnTeSO-2). Ho_2O_3 (0.5 mmol), TeO_2 (0.667 mmol, 0.1064 g), 1 M H_2SO_4 (0.667 mmol, 0.667 mL), and 1.333 mL of H_2O were loaded into a 23 mL PTFE-lined autoclave liner.

$Ln_2TeO_3(SO_4)_2(H_2O)_2$ (Ln = Dy, Ho, and Er; LnTeSO-3). Ln_2O_3 (0.5 mmol; Ln = Dy, Ho, and Er), TeO_2 (0.5 mmol, 0.0798 g), 1 M H_2SO_4 (1 mmol, 1 mL), and 1 mL of H_2O were loaded into a 23 mL PTFE-lined autoclave liner.

$Ln_2(Te_2O_5)(SO_4)_2$ (Ln = Er, Tm, Yb, and Lu; LnTeSO-4). Ln_2O_3 (Ln = Er, Tm, Yb, and Lu; 0.5 mmol), TeO_2 (1 mmol, 0.1596 g), 1 M H_2SO_4 (1 mmol, 1 mL), and 1 mL of H_2O were loaded into a 23 mL PTFE-lined autoclave liner.

$Ln_2(Te_4O_{10})(SO_4)$ (Ln = Gd, Dy, Ho, Er, Tm, and Yb; LnTeSO-5). Ln_2O_3 (Ln = Gd, Dy, Ho, Er, Tm, and Yb; 0.5 mmol), TeO_2 (2 mmol, 0.3192 g), 1 M H_2SO_4 (0.5 mmol, 0.5 mL), and 1.5 mL of H_2O were loaded into a 23 mL PTFE-lined autoclave liner.

The autoclave was sealed and heated to 230 °C for 3 days followed by slow cooling to room temperature at a rate of 5 °C/h. The products were washed with DI water to remove soluble solids, followed by rinsing with ethanol. Photographs of all five sets of crystals can be found in the Supporting Information.

Crystallographic Studies. Single crystals of all of the lanthanide tellurite sulfate compounds were mounted on Mitegen mounts with viscous immersion oil, and optically aligned on a Bruker D8 Quest X-ray diffractometer using a digital camera. Initial intensity measurements were performed using an IμS X-ray source, a 50 W microfocused sealed tube (MoKα, λ = 0.71073 Å) with high-brilliance and high-performance focusing multilayer optics. Standard Quest software was used for determination of the unit cells and data collection control. The intensities of reflections of a hemisphere were collected by a combination of four sets of exposures (frames). Each set had a different φ angle for the crystal, and each exposure covered a range of 0.5° in ω. A total of 1464 frames were collected with an exposure time per frame of 10 to 60 s, depending on the size and quality of the crystal. Quest software was used for data integration including Lorentz and polarization corrections. Semiempirical absorption corrections were applied using the program SADABS or TWINABS.[25] Selected crystallographic information is listed in Table S1. Atomic coordinates and additional structural information are provided in the Supporting Information (CIFs).

Magnetic Property Measurements. The magnetic susceptibilities of lanthanide tellurite sulfates were measured on polycrystalline samples using a superconducting quantum interference device (SQUID) magnetometer (Quantum Design MPMS XL). The DC magnetization was measured in an applied field of 0.1 T in the 1.8−300 K temperature range. Magnetization was also measured with the magnetic field varying from 0 to 5.5 T at 1.8 K. The data was corrected for diamagnetic contributions using Pascal's constants and subtracting the background.[26]

UV−Vis−NIR and Fluorescence Spectroscopy. UV−vis−NIR data were acquired from single crystals using a Craic Technologies microspectrophotometer. Crystals were placed on quartz slides under Krytox oil, and the data were collected from 200 to 1500 nm. The exposure time was auto-optimized by the Craic software. Fluorescence spectra were obtained using 365 nm light for excitation.

RESULTS AND DISCUSSION

Synthesis. The reactions of lanthanide oxides, TeO_2, and H_2SO_4 under hydrothermal conditions yield five series of lanthanide tellurite sulfates with distinct structures. The formation of lanthanide tellurite sulfates is found to be stoichiometrically driven. All of the compounds were obtained as single-phase products with the highest yields (~70%) when the reactants have the same molar ratio of Ln/Te/S as the products.

For **LnTeSO-1** and **LnTeSO-4**,

$$Ln_2O_3(s) + 2TeO_2(s) + 2H_2SO_4(aq) \rightarrow Ln_2(Te_2O_5)(SO_4)_2(s) + 2H_2O(l)$$

For **LnTeSO-2**,

dx.doi.org/10.1021/ic501163x | Inorg. Chem. 2014, 53, 8555−8564

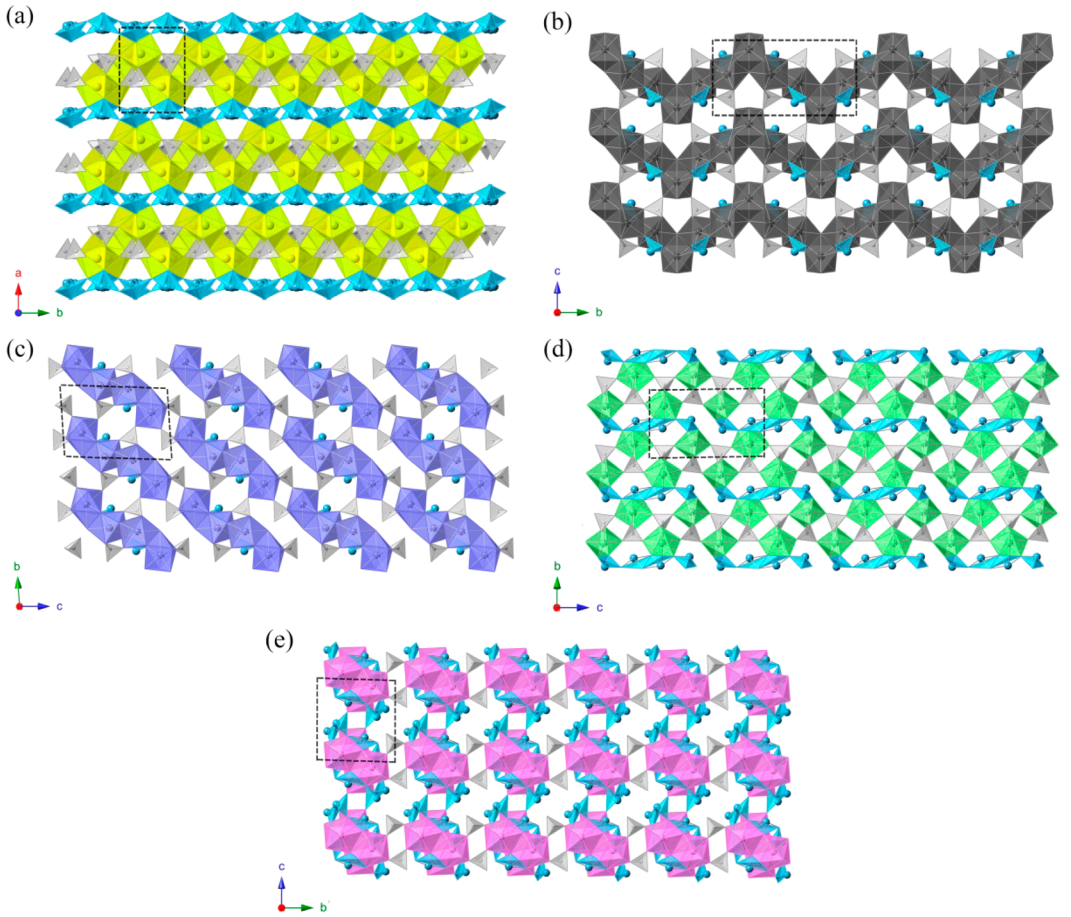

Figure 1. Depiction of the structures of (a) **LnTeSO-1**, (b) **LnTeSO-2**, (c) **LnTeSO-3**, (d) **LnTeSO-4**, and (e) **LnTeSO-5**. Lanthanide polyhedra are shown in yellow, dark gray, purple, green, and pink in **LnTeSO-1**, **LnTeSO-2**, **LnTeSO-3**, **LnTeSO-4**, and **LnTeSO-5**, respectively. Tellurite polyhedra in blue, and sulfate tetrahedra in light gray.

$$3Ho_2O_3(s) + 4TeO_2(s) + 4H_2SO_4(aq) \rightarrow 2Ho_3(TeO_3)_2(SO_4)_2(OH)(H_2O)(s) + H_2O(l)$$

For **LnTeSO-3**,

$$Ln_2O_3(s) + TeO_2(s) + 2H_2SO_4(aq) \rightarrow Ln_2TeO_3(SO_4)_2(H_2O)_2(s)$$

For **LnTeSO-5**

$$Ln_2O_3(s) + 4TeO_2(s) + H_2SO_4(aq) \rightarrow Ln_2(Te_4O_{10})(SO_4)(s) + H_2O(l)$$

Structures and Topological Descriptions. Single crystal X-ray diffraction reveals that the early lanthanide compounds **LnTeSO-1** (Ln = La, Ce, Pr, Nd, Sm, Eu, Gd, Tb) crystallize in a monoclinic space group $P2_1/c$. The Ce compound has been reported in our previous study for which detailed structural information is available, but the analogues reported here result from this work.[9a] These compounds form dense three-dimensional (3D) structures as shown in Figure 1a. The 3D framework is composed of Ln−oxo sheets, tellurite layers, and sulfates. The Ln center is an approximately tricapped trigonal prism where six O atoms are donated from SO_4^{2-} anions and three O atoms from tellurite anions (cf. Figure 3a). The average Ln−O bond length decreases from 2.55 Å for La to 2.44 Å for Tb. This trend is consistent with the increasing localization and decreased shielding of the 4f orbitals given the consequent ionic contraction. The LnO_9 polyhedra share three edges with three other Ln centers, forming a zigzagging two-dimensional (2D) Ln−oxo sheet topology (cf. Figure 2a). Within the tellurite layer, Te atoms are highly disordered and delocalized into two Te atoms with a total occupancy of 1.

LnTeSO-2 (Ln = Ho) crystallizes in the monoclinic space group of $P2_1/m$ featuring a 3D framework as shown in Figure 1b. The main feature of this structure is the one-dimensional (1D) Ho−oxo chains that extend along the *b* axis. The chains are polymerized from Ho polyhedra into a zigzagging structure, and an [*ab*] plane view of the chains is shown in Figure 2b. The Ho−oxo chains contain two crystallographically unique Ho^{3+} ions. The face-sharing Ho(1)−O−Ho(2) bonding presents one short Ho(1)−Ho(2) distance of 3.5339(5) Å. The edge-sharing Ho(1)−O−Ho(1) bonding shows a relatively long Ho(1)−Ho(1) distance of 3.7811(6) Å (cf. Figure S2b). Both Ho^{3+} centers are coordinated with eight O atoms, forming square antiprisms with approximate D_{4d} symmetry (cf. Figure 3b). The average Ho−O bond length is 2.37 Å for Ho(1) and 2.36 Å for Ho(2). TeO_3^{2-} and SO_4^{2-} moieties bridge those 1D chains into a 3D framework. The remaining positive charge needed to counterbalance the anionic framework is accomplished by protonating the O(8) and O(9), based on bond valence sum (BVS) calculations.[27]

The structure of **LnTeSO-3** (Ln = Dy, Ho, and Er) is based on 3D framework with a triclinic space group of $P\bar{1}$. **LnTeSO-3**

dx.doi.org/10.1021/ic501163x | *Inorg. Chem.* 2014, 53, 8555−8564

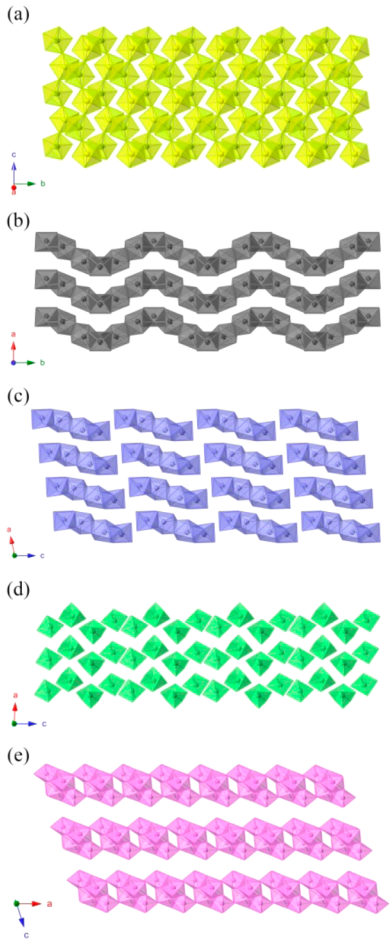

Figure 2. Depiction of the structures of (a) **LnTeSO-1**, (b) **LnTeSO-2**, (c) **LnTeSO-3**, (d) **LnTeSO-4**, and (e) **LnTeSO-5** showing the linking of Ln polyhedra bridged by oxygen atoms. Lanthanide polyhedra are shown in yellow, dark gray, purple, green, and pink in **LnTeSO-1**, **LnTeSO-2**, **LnTeSO-3**, **LnTeSO-4**, and **LnTeSO-5**, respectively.

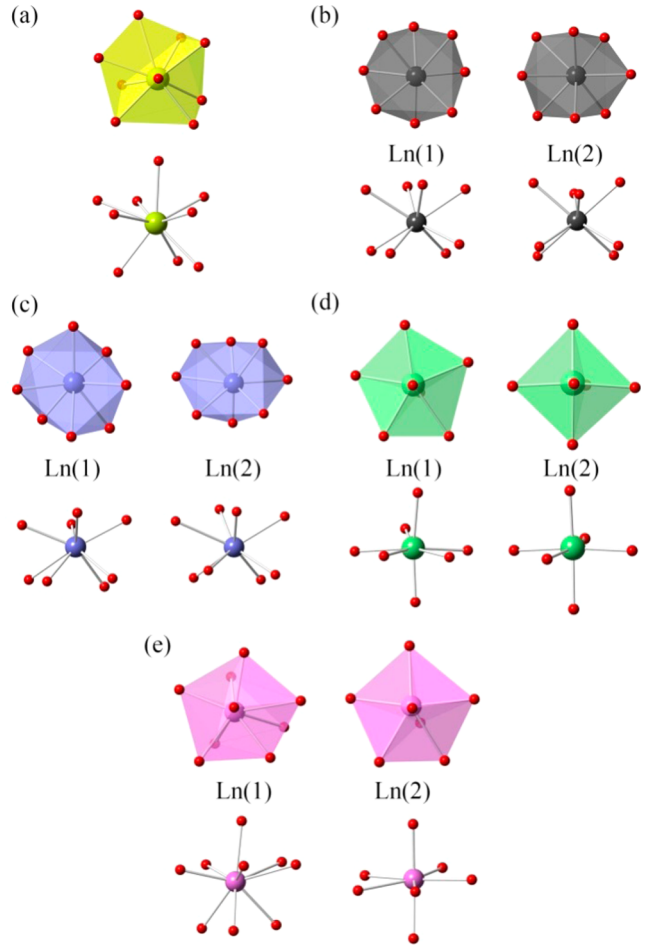

Figure 3. Views of the coordination geometries of lanthanide ions in (a) **LnTeSO-1**, (b) **LnTeSO-2**, (c) **LnTeSO-3**, (d) **LnTeSO-4**, and (e) **LnTeSO-5**. Lanthanide polyhedra are shown in yellow, dark gray, purple, green, and pink in **LnTeSO-1**, **LnTeSO-2**, **LnTeSO-3**, **LnTeSO-4**, and **LnTeSO-5**, respectively. O atoms are in red.

is composed of Ln-oxo tetramers and TeO_3^{2-} and SO_4^{2-} polyhedra (cf. Figure 1c). The tetramers are shown in Figure 2c, and each of them contains two independent Ln^{3+} centers, Ln(1) and Ln(2). The terminal Ln(2) polyhedra share one face with bridging Ln(1) polyhedra, and Ln(1) share one edge with another Ln(1) (cf. Figure S2c). The face-sharing bonding presents a short Ln(1)−Ln(2) distance of 3.6970(6) Å for Dy, 3.6790(6) Å for Ho, and 3.647(2) Å for Er. The edge-sharing bonding shows a Ln(1)−Ln(1) distance of 3.8306(8) Å for Dy, 3.8123(8) Å for Ho, and 3.787(3) Å for Er. Both Ln centers adopt an eight-coordinate environment with square antiprismic geometry, and O atoms bound to Ln are donated from tellurite or sulfate anions.

The **LnTeSO-4** (Ln = Er, Tm, Yb, Lu) compounds have an identical molecular formula to that of **LnTeSO-1** but crystallize in the lower symmetry space group $P\bar{1}$. As depicted in Figure 1d, **LnTeSO-4** exhibits a 3D framework consisting of Ln polyhedra, $Te_4O_{10}^{4-}$ polymers, and SO_4^{2-} anions. Instead of polymerizing into a 2D sheet, 1D chain, or polymer, Ln polyhedra exist as monomers in the structure (cf. Figure 2d). The most remarkable feature of **LnTeSO-4** is the coordination environments of the Ln^{3+} ions. In **LnTeSO-4**, rare pentagonal bipyramid Ln(1) and uncommon octahedral Ln(2) centers were found (cf. Figure 3d). The pentagonal bipyramidal geometry is very common for neptunyl and uranyl owing to the presence of short, terminal oxo bounds; however, it is quite rare in trivalent lanthanides because of the large degree of anisotropy.[28] The capping oxygen atoms have relatively short Ln−O bond lengths, 2.136(8) and 2.268(7) Å for Er, 2.103(3) and 2.240(4) Å for Tm, 2.098(3) and 2.215(3) Å for Yb, and 2.100(5) and 2.217(5) Å for Lu. The equatorial Ln−O bond distances range from 2.298(8) Å to 2.444(7) Å, 2.274(3) Å to 2.436(4) Å, 2.284(3) Å to 2.429(3) Å, and 2.255(5) Å to 2.415(5) Å for Er, Tm, Yb, and Lu analogues, respectively (cf. Table S2). Octahedral geometry is quite common for 3d transition metal and sometimes can be found in lanthanide−halide moieties, but its representation in the literature for Ln−oxo based compounds is sparse.[29] The average Ln(2)−O bond lengths are 2.23, 2.21, 2.21, and 2.20 Å for Er, Tm, Yb, and Lu, respectively.

LnTeSO-5 (Ln = Gd, Dy, Ho, Er, Tm, and Yb) exhibits a 3D framework with a triclinic space group of $P\bar{1}$ and is composed of two crystallographically independent Ln^{3+} ions, $Te_4O_{10}^{4-}$ polynuclear clusters, and SO_4^{2-}. A view of the structure is shown in Figure 1e. Ln(1) and Ln(2) polyhedra in **LnTeSO-5** edge-share and face-share with each other, forming a tetramer unit (cf. Figure S2e). Those tetramer units are further bridged along the *a* axis, forming a chain structure (Figure 2e). Ln(1)

dx.doi.org/10.1021/ic501163x | *Inorg. Chem.* 2014, 53, 8555−8564

has the same nine-coordinate tricapped trigonal prismatic geometry as observed in **LnTeSO-1**, and Ln(2) features a pentagonal bipyramidal geometry (Figure 3e). Tellurites have rich structural chemistry attributable to their stereochemically active lone-pair electrons as well as their variable coordination environments. The ability of Te^{IV} to bind to three, four, or even five O atoms enables tellurites to form diverse substructures including 1D chains, 2D layers, and 3D frameworks.[23a] In this work, a novel 3D $Te_4O_{10}^{4-}$ network is found in **LnTeSO-5**. Within those four crystallographically unique Te^{4+} ions, Te(1) is found as the classical trigonal pyramid being bound by three oxygen atoms; whereas Te(2), Te(3), and Te(4) four-coordinate with dispenoid coordination environments. Each tellurite polyhedra corner-shares with two other tellurite forming an eight-membered tellurite ring with an inversion center (cf. Figure S3).

Periodic Trends. The lanthanide contraction is clearly observed in these lanthanide tellurite sulfates. The effects of lanthanide contraction is reflected in the decreasing volume of the unit cells in the same structure type (cf. Table S1), decreasing Ln−O bonding distance (cf. Table S2), decreasing coordination number of the lanthanides, and more dramatically in the change in topology. From **LnTeSO-1**, **LnTeSO-2**, **LnTeSO-3**, to **LnTeSO-4**, we observe the following transitions: (1) The Ln−oxo bonding topologies change from a 2D layer (**LnTeSO-1**) → 1D chain (**LnTeSO-2**) → tetrameter (**LnTeSO-3**) and finally to monomer (**LnTeSO-4**). (2) The coordination numbers of lanthanides decrease from nine (**LnTeSO-1**) → eight (**LnTeSO-2** and **LnTeSO-3**) → seven and six (**LnTeSO-4**). Raymond's study suggests that the inverse of lanthanide ionic radii as a function of f electron number gives a very good linear fit for a variety of lanthanide complexes.[30] The ionic radii of Ln^{3+} in these lanthanide tellurite sulfates were obtained by subtracting the ionic radius of O^{2-} ions from the Ln−O distances. Almost linear trends relating Ln ionic radius versus the numbers of f electrons were observed for **LnTeSO-1**, **LnTeSO-3**, and **LnTeSO-4**, respectively (cf. Figure 4). To adopt the same structure as the **LnTeSO-1**, an ionic radius of 0.96 Å is needed for Lu, based on the equation $y = 0.0112x + 0.8706$. The effective ionic radius for nine-coordinate Lu^{3+} is 1.172 Å.[31] The crystal lattice of **LnTeSO-1** is experiencing increasing strain with decreasing ionic radius, resulting in the phase transitions for the late lanthanides.

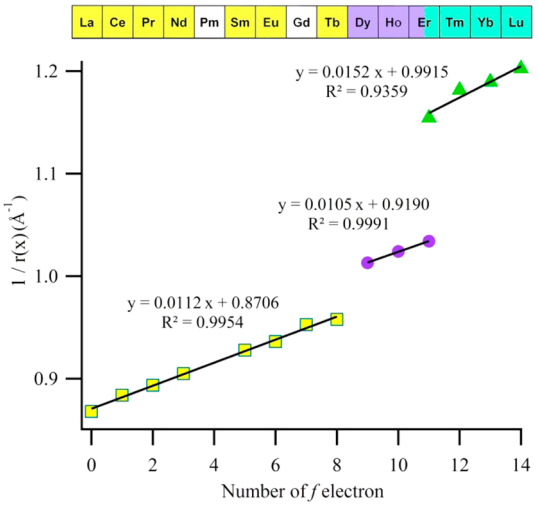

Figure 4. Plot of the inverse of the ionic radii vs the number of the f electrons for **LnTeSO-1** (yellow), **LnTeSO-3** (purple), and **LnTeSO-4** (green).

Magnetic Properties. Owing to the magnetic interactions that could arise as a result of the presence of 4f unpaired electrons and multiple bonding geometries between the lanthanide ions, dc magnetic-susceptibility studies were performed. Some lanthanide tellurite sulfates were not included in this study owing to the low yield or the presence of impurities.

***LnTeSO-1** (Ln = Ce, Pr, and Nd).* Temperature dependence of χ, χ^{-1} (inset), χT and field dependence of magnetization at 1.8 K for $Ce_2(Te_2O_5)(SO_4)_2$, $Pr_2(Te_2O_5)(SO_4)_2$, and $Nd_2(Te_2O_5)(SO_4)_2$ are shown in Figure 5. Above 100 K, the inverse susceptibilities (χ^{-1}) for the Ce, Pr, and Nd analogues obey the modified Curie−Weiss law, $1/\chi = 1/[\chi_{TIP} + C/(T - \theta)]$, where C, θ, and χ_{TIP} represent the Curie constant, the Weiss temperature, and the temperature independent paramagnetic (TIP) contributions, respectively. The negative Weiss temperatures (Table 1) indicate prevailing antiferromagnetic interactions between the nearest-neighbor ions. The effective moment is evaluated from the Curie constant, $C = N\mu_{eff}^2\mu_B^2/3k_B$, where N, μ_B, and k_B are Avogadro's number, Bohr magneton, and Boltzmann constant, respectively. The effective moment is equal to 2.41 μ_B, 3.76 μ_B, and 3.70 μ_B for **CeTeSO-1**, **PrTeSO-1**, and **NdTeSO-1**, which is in great agreement with the theoretical value of 2.54 μ_B for Ce^{3+} ($^2F_{5/2}$, $J = 5/2$, $g = 6/7$), 3.58 μ_B for Pr^{3+} ($^3H_4$, $J = 4$, $g = 4/5$), and 3.62 μ_B for Nd^{3+} ($^4I_{9/2}$, $J = 9/2$, $g = 8/11$). The antiferromagnetic exchange is further supported by the suppressed magnetization values as compared to the sum of Brillouin functions for two Ln^{3+} ions at 1.8 K and the decrease in the χT value at lower temperatures. The field-dependent magnetization for $Pr_2(Te_2O_5)(SO_4)_2$ is unusual with respect to the Ce and Nd analogues; it adopts a linear behavior with a relatively small maximum value (1.62 μ_B). This finding suggests that the Pr^{3+} is close to antiferromagnetic ordering that might occur at slightly lower temperatures than that available in our experiment.

***LnTeSO-1** (Ln = Sm).* The Sm^{3+} ion is well-known to show Van Vleck paramagnetism owing to the presence of low-lying excited states.[12b] Consequently, the inverse susceptibility plot for $Sm_2(Te_2O_5)(SO_4)_2$ exhibits strong deviation from the Curie−Weiss law (Figure 6). As the sample is cooled down, the depopulation of excited states leads to the continuous decrease in χT at lower temperatures with an approximately linear relationship. No magnetic phase transition was observed for $Sm_2(Te_2O_5)(SO_4)$ down to 1.8 K due to the paramagnetic ground state of the Sm^{3+} ions ($^6H_{5/2}$). Nevertheless, the field-dependent magnetization measured at 1.8 K shows a similar linear behavior as in $Pr_2(Te_2O_5)(SO_4)$, with a maximum value of 0.27 μ_B, suggesting that antiferromagnetic ordering could be observed at a slightly lower temperature which is out of the range of this study.

***TbTeSO-1**.* This compound exhibits linear Curie−Weiss behavior in the χ^{-1} vs T data nearly in the entire 75−300 K temperature range with a positive Weiss temperature 9.9(5) K (Figure 7 inset), indicating a ferromagnetic exchange coupling between nearest Tb^{3+} ions. The effective moment is equal to 10.69 μ_B, which is comparable with the theoretical value of 9.72 μ_B for Tb^{3+} ($^7F_6$, $J = 6$, $g = 3/2$). The χT value of **TbTeSO-1** increases steadily with the decreasing temperature from 300 to 10 K, followed by the sharp increase from 10 to 1.8 K. This is another indicator of short-range ferromagnetic correlations

dx.doi.org/10.1021/ic501163x | Inorg. Chem. 2014, 53, 8555−8564

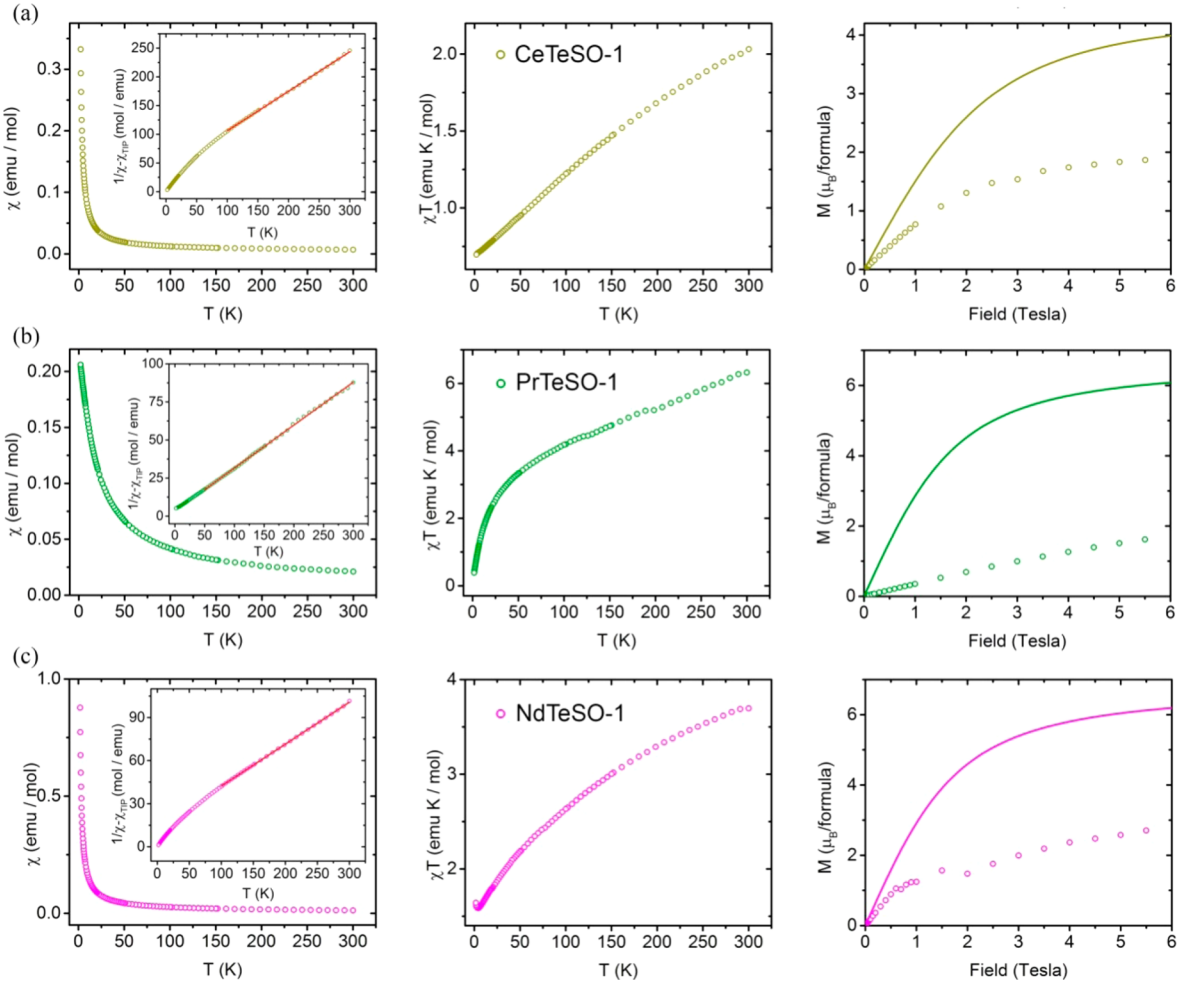

Figure 5. Temperature dependence of χ, χ^{-1} (inset), χT, and field dependence of magnetization at 1.8 K for (a) $Ce_2(Te_2O_5)(SO_4)_2$, (b) $Pr_2(Te_2O_5)(SO_4)_2$ and (c) $Nd_2(Te_2O_5)(SO_4)_2$, respectively. The solid red line in χ^{-1} (inset) shows the fit to the Curie–Weiss law, while the solid lines in plots of magnetization vs field represent the magnetization calculated as the sum of Brillouin functions for two Ln^{3+} ions.

Table 1. Magnetic Data for Lanthanide Tellurite Sulfates

	Curie–Weiss fitting			
			μ_{eff} (RE^{3+},μ_B)	
comp.	C (emu·K·mol^{-1})	θ (K)	from C	theo.
Ce-1	1.453(5)	−54(8)	2.41	2.54
Pr-1	3.54(5)	−12(1)	3.76	3.58
Nd-1	3.42(7)	−44(2)	3.70	3.62
Sm-1				0.84
Tb-1	28.6(1)	9.9(5)	10.69	9.72
Gd-5	17.75(4)	−7.7(4)	8.42	7.94
Dy-5	29.25(1)	−4.26(9)	10.81	10.63
Ho-5	31.86(2)	−8.4(2)	11.29	10.60
Er-4	23.22(1)	−8.28(9)	9.64	9.59
Er-5	22.73(2)	−4.1(1)	9.53	9.59
Tm-4	15.93(3)	−4.2(3)	7.98	7.57
Tm-5	16.72(3)	−15.8(4)	8.18	7.57
Yb-4	5.64(2)	−58.6(9)	4.75	4.54

between the Tb^{3+} magnetic moments. The field-dependent magnetization measured at 1.8 K shows a sharp increase of magnetization at low field. Below 0.75 T, the magnetization value is larger than the sum of Brillouin functions for two Tb^{3+} ions in the absence of magnetic exchange, which indicates that there is ferromagnetic ordering around 1.8 K. Nonetheless, at fields above 0.75 T the magnetization increases much slower than expected from the Brillouin function, which can be explained by the population of low-lying excited states.

LnTeSO-5 *(Ln = Gd, Dy, Ho).* For all these compounds, the temperature dependence of χ^{-1} follows the Curie–Weiss law in the 1.8–300 K range (Figure 8). All of these compounds are paramagnetic with antiferromagnetic correlations between the neighboring Ln^{3+}, which is supported by the slightly negative Weiss temperatures (Table 1) and the decrease in the χT value at lower temperatures. Gd^{3+} has the largest spin moment (S = 7/2), while the orbital momentum vanishes (L = 0).[12b] There is no anisotropy of the charge and correspondingly no crystal field splitting. Consequently, the magnetization of **GdTeSO-5** has good agreement with the sum of Brillouin functions for two free Gd^{3+} ions. The suppressed magnetizations for **DyTeSO-5** and **HoTeSO-5** as compared to the sum of Brillouin functions for two free Ln^{3+} ions could be attributed to the crystal electric field splitting and possibly antiferromagnetic interactions between Ln^{3+} ions. The effective magnetic moments per RE^{3+} ion are 8.42 μ_B, 10.81 μ_B, and 11.29 μ_B for Gd^{3+}, Dy^{3+}, and Ho^{3+} respectively, matching well with the theoretical values 7.94 μ_B, 10.63 μ_B, and 10.60 μ_B for Gd^{3+} ($^8S_{7/2}$, J = 7/2, g = 2), Dy^{3+} ($^6H_{15/2}$, J = 15/2, g = 4/3), and Ho^{3+} ($^5I_8$, J = 8, g = 5/4), respectively.

dx.doi.org/10.1021/ic501163x | Inorg. Chem. 2014, 53, 8555–8564

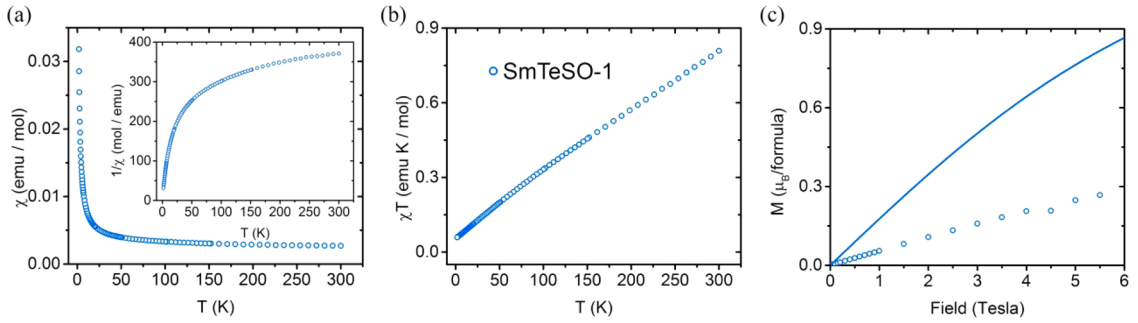

Figure 6. Temperature dependence of (a) χ and χ^{-1} (inset), (b) χT, and (c) field dependence of magnetization at 1.8 K for $Sm_2(Te_2O_5)(SO_4)_2$.

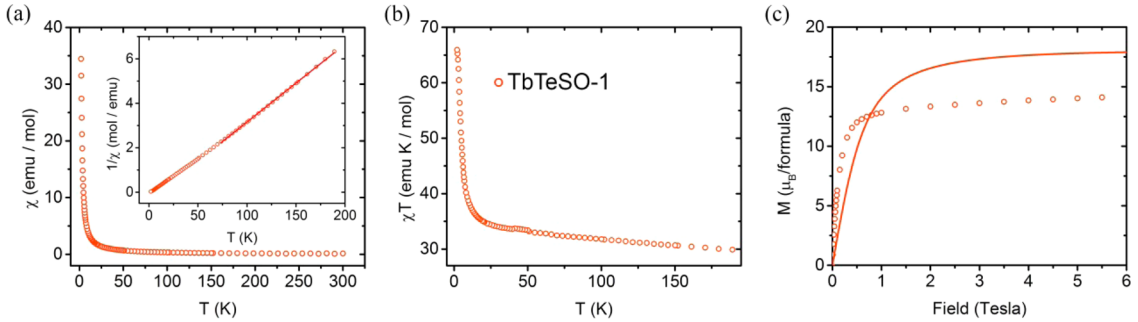

Figure 7. Temperature dependence of (a) χ and χ^{-1} (inset), (b) χT, and (c) field dependence of magnetization at 1.8 K for $Tb_2(Te_2O_5)(SO_4)_2$.

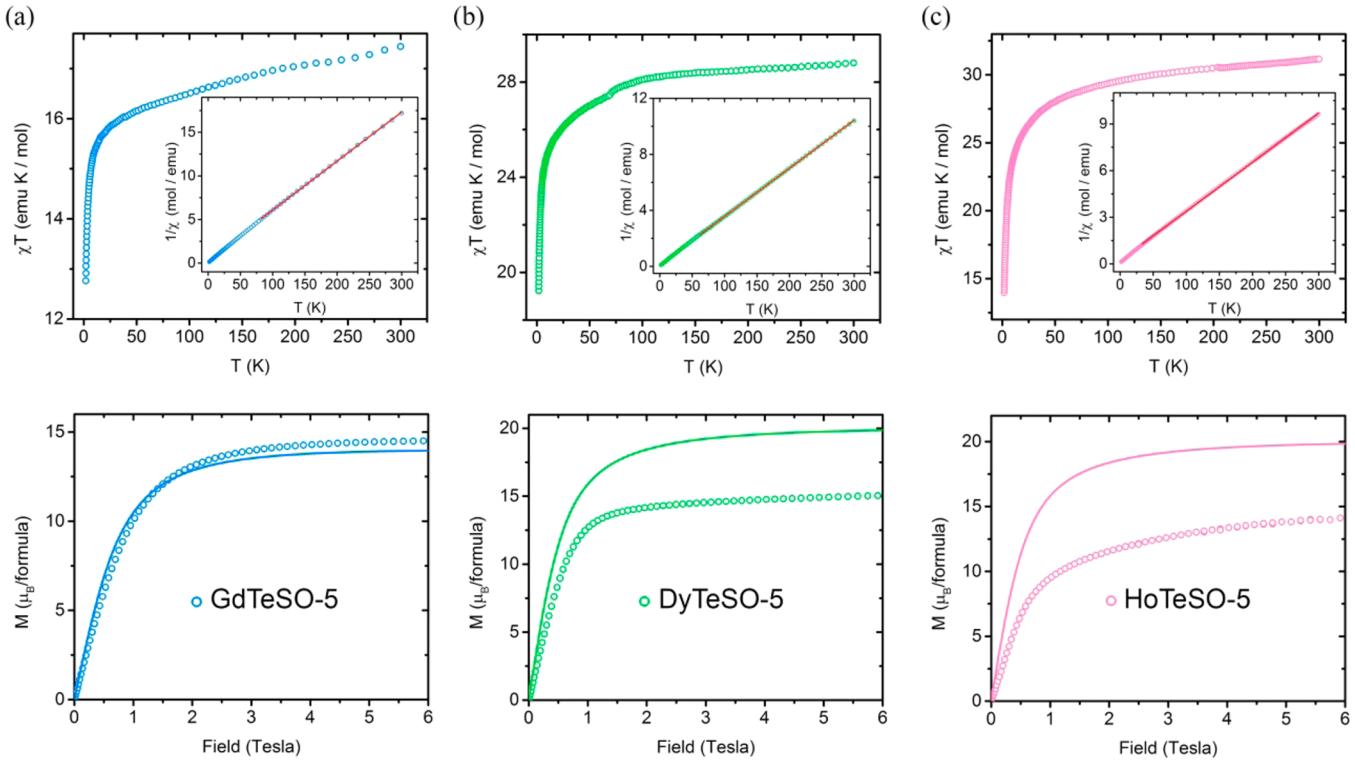

Figure 8. Temperature dependence of χT, χ^{-1} (inset), and field dependence of magnetization at 1.8 K for (a) **GdTeSO-5**, (b) **DyTeSO-5**, and (c) **HoTeSO-5**.

LnTeSO-4 and LnTeSO-5 *(Ln = Er and Tm).* Both **LnTeSO-4** and **LnTeSO-5** contain two crystallographically independent Ln^{3+} ions, but their structures are completely different. The Ln polyhedra in **LnTeSO-4** exist as zero-dimensional monomers in the structure. Ln(1) and Ln(2) polyhedra in **LnTeSO-5**, however, edge-share and face-share with each other, forming a tetramer unit. The nearest Ln−Ln distances are 5.142(7) and 5.112(5) for **ErTeSO-4** and **TmTeSO-4**, compared to those of 3.6849(7) and 3.6915(9) for **ErTeSO-5** and **TmTeSO-5**, respectively (Table S3). It would be interesting to examine the effects of structure differences as they relate to magnetic behaviors. As shown in

dx.doi.org/10.1021/ic501163x | Inorg. Chem. 2014, 53, 8555−8564

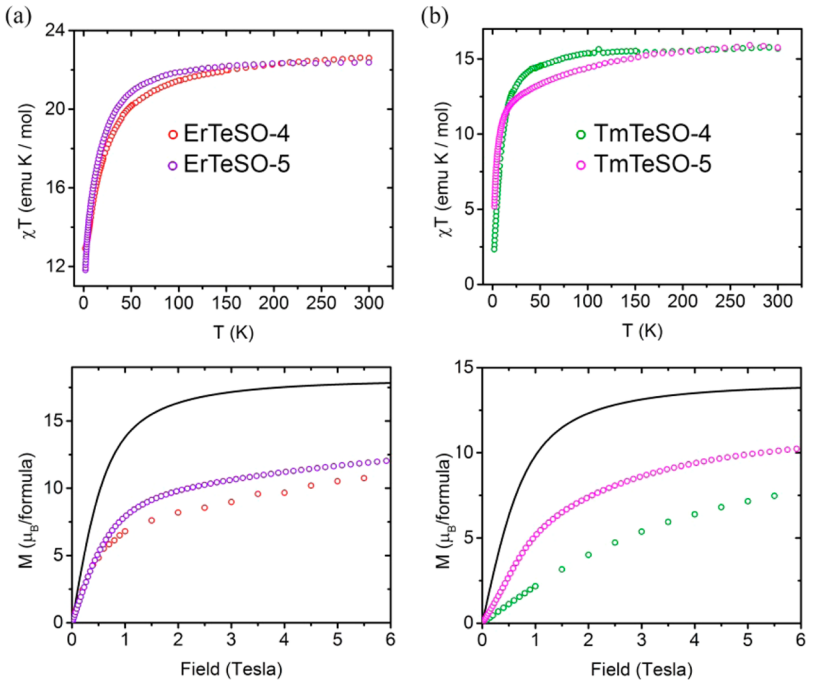

Figure 9. Temperature dependence of χT and field dependence of magnetization at 1.8 K for (a) **ErTeSO-4** and **EreSO-5** and (b) **TmTeSO-4** and **TmTeSO-5**.

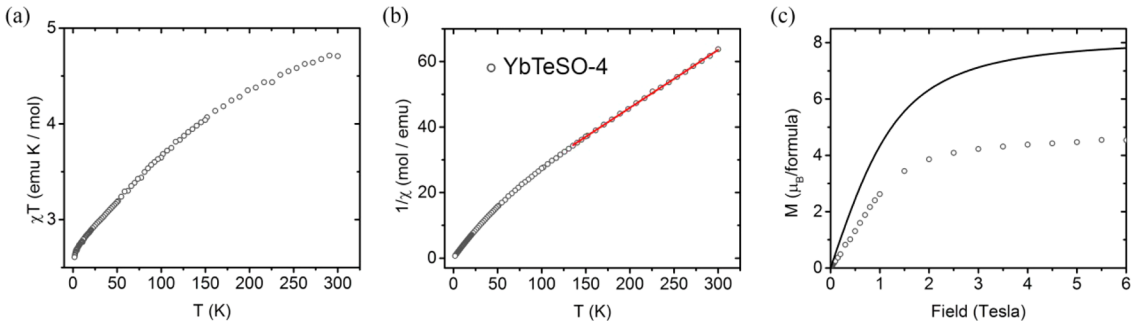

Figure 10. Temperature dependence of (a) χT, (b) χ^{-1}, and (c) field dependence of magnetization at 1.8 K for **YbTeSO-4**.

Figure 9a, the χT values for **ErTeSO-4** and **ErTeSO-5** showed values of 22.60 emu·K·mol^{-1} and 22.37 emu·K·mol^{-1} at 300 K, which agree with the theoretical value 23.00 emu·K·mol^{-1} of two ground state Er^{3+} ($^4I_{15/2}$, J = 15/2, g = 6/5, 22.96 emu·K·mol^{-1}). The values of χT at 300 K are 15.69 emu·K·mol^{-1} for **TmTeSO-4** and 15.75 emu·K·mol^{-1} for **TmTeSO-5**, which is also in reasonable agreement with the expected value 14.33 emu·K·mol^{-1} for the free Tm^{3+} ion ($^3H_6$, J = 6, g = 7/6). The χT values decreased on cooling and deviations of χT values between two structures were observed from 5 to 200 K, which could be attributed to the different crystal fields. The field-dependent magnetization measured at 1.8 K shows that all four compounds have a lower magnetization than the sum of Brillouin functions for two Er^{3+} or Tm^{3+} ions in the absence of magnetic exchange, which further confirmed the presence of crystal electric field splitting. **LnTeSO-5** has relatively higher magnetization than that of **LnTeSO-4**, suggesting a stronger crystal electric field splitting in the structure type **LnTeSO-5**.

LnTeSO-4 *(Ln = Yb).* Despite crystallizing as an isotypic structure as the other **LnTeSO-4** (Ln = Er and Tm) compounds, **YbTeSO-4** behaves differently than the two analogues just described. Figure 10 shows temperature dependence of the χT value. The χT drops off gradually with decreasing temperatures, suggesting the existence of antiferromagnetic interactions. Both χT vs T and M vs H plots support the presence of short-range antiferromagnetic exchange. The antiferromagnetic exchange is further supported by the suppressed magnetization values as compared to the sum of Brillouin functions for two Yb^{3+} ions, as well as the negative Weiss temperature, $\theta = -58.6(9)$ K. The effective moment is equal to 4.75 μ_B, which matches with the theoretical value of 4.54 μ_B for Yb^{3+} ($^2F_{7/2}$, J = 7/2, g = 8/7). The $1/\chi$ vs T plot represents a linear relationship from 150 to 300 K, followed by curvature below 150 K.

UV–Vis–NIR and Photoluminescence Spectroscopy. The emission spectra of $Eu_2(Te_2O_5)(SO_4)_2$ and $Tb_2(Te_2O_5)(SO_4)_2$ at the excited wavelength of 315 nm exhibit the characteristic emission of Eu^{3+} and Tb^{3+}, respectively. The **EuTeSO-1** and **TbTeSO-1** crystals fluoresce with sufficient intensity that the emission from a few crystals is easily observed by the naked eye, as shown in Figure 11. The photoemission spectrum **EuTeSO-1** shows three typical vibronic bands, which can be attributed to $^5D_0 \rightarrow {}^7F_1$ (589 nm), $^5D_0 \rightarrow {}^7F_2$ (613 nm), and $^5D_0 \rightarrow {}^7F_4$ (698 nm; cf. Figure 11).[32] $Tb_2(Te_2O_5)(SO_4)_2$ shows a typical emission spectrum with four vibronic bands $^5D_4 \rightarrow {}^7F_6$ (489 nm), $^5D_4 \rightarrow {}^7F_5$ (543 nm), $^5D_4 \rightarrow {}^7F_4$ (585 nm),

dx.doi.org/10.1021/ic501163x | Inorg. Chem. 2014, 53, 8555–8564

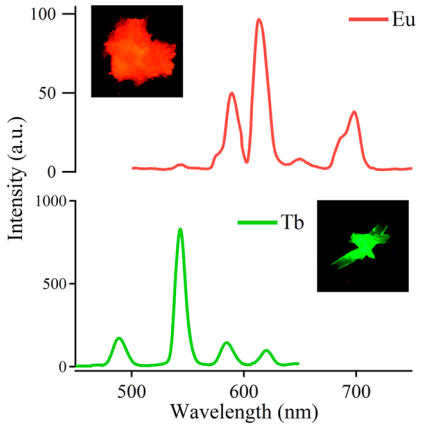

Figure 11. Photoluminescence spectra of $Eu_2(Te_2O_5)(SO_4)_2$ and $Tb_2(Te_2O_5)(SO_4)_2$.

and $^5D_4 \rightarrow {}^7F_3$ (620 nm).[33] The solid state UV−vis−NIR absorbance spectra of all lanthanide tellurite sulfates were obtained from single crystals and are shown in Figure S4. All of the compounds show absorbance from approximately 250 to 350 nm, which can be ascribed to the Te−O charge transfer based on the measurement of the TeO_2 crystal. The electronic transitions of 4f elements have been characterized in the literature, and the signature peaks of trivalent lanthanides are displayed in their respective spectrum.[34]

CONCLUSIONS

The **LnTeSO-1**, **LnTeSO-2**, **LnTeSO-3**, **LnTeSO-4**, and **LnTeSO-5** provide examples of an isomorphous series spanning the entire 4f block (except *Pm*). The lanthanide contraction results in completely different topologies of **LnTeSO-1**, **LnTeSO-2**, **LnTeSO-3**, **LnTeSO-4**, and **LnTeSO-5**. For the first four topologies, the Ln−oxo bonding geometries transit from a 2D layer (**LnTeSO-1**) → 1D chain (**LnTeSO-2**) → tetrameter (**LnTeSO-3**) and finally to a monomer (**LnTeSO-4**), with the coordination numbers of lanthanide centers decreasing from nine (**LnTeSO-1**) → eight (**LnTeSO-2** and **LnTeSO-3**) → seven and six (**LnTeSO-4**). No magnetic phase transitions were observed for any of the materials with paramagnetic Ln^{3+} ions above 1.8 K despite the presence of short Ln···Ln distances. Nevertheless, **LnTeSO-1** unveils switching of magnetic behavior from short-range antiferromagnetic correlations for **CeTeSO-1**, **PrTeSO-1**, and **NdTeSO-1** to ferromagnetic interactions present in **TbTeSO-1**. The structural diversity of **LnTeSO-4** and **LnTeSO-5** is reflected by the slight change of the magnetic properties for the Er and Tm analogues. A stronger crystal electric field splitting in structure type **LnTeSO-5** was observed.

ASSOCIATED CONTENT

Supporting Information

X-ray crystallographic files in CIF format; table of crystallographic data, table for selected bond distances, and table of the closest Ln^{3+}−Ln^{3+} distances; and Figures S1, S2, S3, and S4 are shown. This material is available free of charge via the Internet at http://pubs.acs.org.

AUTHOR INFORMATION

Corresponding Author

*E-mail: albrecht-schmitt@chem.fsu.edu.

Notes

The authors declare no competing financial interest.

ACKNOWLEDGMENTS

This material is based upon work supported as part of the Materials Science of Actinides, an Energy Frontier Research Center funded by the U.S. Department of Energy, Office of Science, Office of Basic Energy Sciences under Award Number DE-SC0001089. This work was supported by a Chinese Scholarship Council Graduate Fellowship to J.L.

REFERENCES

(1) Masset, A. C.; Michel, C.; Maignan, A.; Hervieu, M.; Toulemonde, O.; Studer, F.; Raveau, B.; Hejtmanek, J. *Phys. Rev. B* **2000**, *62*, 166−175.
(2) Maeno, Y.; Hashimoto, H.; Yoshida, K.; Nishizaki, S.; Fujita, T.; Bednorz, J. G.; Lichtenberg, F. *Nature* **1994**, *372*, 532−534.
(3) Eaton, T.; Lin, J.; Cross, J. N.; Stritzinger, J. T.; Albrecht-Schmitt, T. E. *Chem. Commun.* **2014**, *50*, 3668−3670.
(4) (a) Zhong, X. C.; Zou, M.; Zhang, H.; Liu, Z. W.; Zeng, D. C.; Gschneidner, K. A., Jr.; Pecharsky, V. K. *J. Appl. Phys.* **2011**, *109*, 07A917/911−907A917/913. (b) Ritter, C.; Provino, A.; Manfrinetti, P.; Gschneidner, K. A., Jr. *J. Alloys Compd.* **2011**, *509*, 9724−9732. (c) Mudryk, Y.; Manfrinetti, P.; Smetana, V.; Liu, J.; Fornasini, M. L.; Provino, A.; Pecharsky, V. K.; Miller, G. J.; Gschneidner, K. A., Jr. *J. Alloys Compd.* **2013**, *557*, 252−260. (d) Levin, E. M.; Pecharsky, V. K.; Gschneidner, K. A., Jr. *J. Appl. Phys.* **2001**, *90*, 6255−6262. (e) Clatterbuck, D. M.; Lange, R. J.; Gschneidner, K. A., Jr. *J. Magn. Magn. Mater.* **1999**, *195*, 639−645. (f) Clatterbuck, D. M.; Gschneidner, K. A., Jr. *J. Magn. Magn. Mater.* **1999**, *207*, 78−94.
(5) Lin, J.; Chai, P.; Diefenbach, K.; Shatruk, M.; Albrecht-Schmitt, T. E. *Chem. Mater.* **2014**, *26*, 2187−2194.
(6) Polinski, M. J.; Grant, D. J.; Wang, S.; Alekseev, E. V.; Cross, J. N.; Villa, E. M.; Depmeier, W.; Gagliardi, L.; Albrecht-Schmitt, T. E. *J. Am. Chem. Soc.* **2012**, *134*, 10682−10692.
(7) Cotton, S. *Lanthanide and Actinide Chemistry*; Wiley: New York, 2006.
(8) Beineke, T. A.; Delgaudio, J. *Inorg. Chem.* **1968**, *7*, 715−721.
(9) (a) Lin, J.; Cross, J. N.; Diwu, J.; Meredith, N. A.; Albrecht-Schmitt, T. E. *Inorg. Chem.* **2013**, *52*, 4277−4281. (b) Lin, J.; Cross, J. N.; Diwu, J.; Polinski, M. J.; Villa, E. M.; Albrecht-Schmitt, T. E. *Inorg. Chem.* **2012**, *51*, 11949−11954. (c) Lin, J.; Diwu, J.; Cross, J. N.; Villa, E. M.; Albrecht-Schmitt, T. E. *Inorg. Chem.* **2012**, *51*, 10083−10085.
(10) Polinski, M. J.; Garner, E. B., III; Maurice, R.; Planas, N.; Stritzinger, J. T.; Parker, T. G.; Cross, J. N.; Green, T. D.; Alekseev, E. V.; Van Cleve, S. M.; Depmeier, W.; Gagliardi, L.; Shatruk, M.; Knappenberger, K. L.; Liu, G.; Skanthakumar, S.; Soderholm, L.; Dixon, D. A.; Albrecht-Schmitt, T. E. *Nat. Chem.* **2014**, *6*, 387−392.
(11) (a) Sankar, S. G.; Rao, V. U. S.; Segal, E.; Wallace, W. E.; Frederick, W. G. D.; Garrett, H. J. *Phys. Rev. B* **1975**, *11*, 435−439. (b) Herbst, J. F.; Croat, J. J.; Pinkerton, F. E.; Yelon, W. B. *Phys. Rev. B* **1984**, *29*, 4176−4178.
(12) (a) Carlin, R. L. *Magnetochemistry*; Springer-Verlag: Berlin, 1986. (b) Buschow, K. H. J.; De Boer, F. R. *Physics of Magnetism and Magnetic Materials*; Springer: London, 2012.
(13) Rinehart, J. D.; Long, J. R. *Chem. Sci.* **2011**, *2*, 2078−2085.
(14) Long, J.; Habib, F.; Lin, P.-H.; Korobkov, I.; Enright, G.; Ungur, L.; Wernsdorfer, W.; Chibotaru, L. F.; Murugesu, M. *J. Am. Chem. Soc.* **2011**, *133*, 5319−5328.
(15) Sorace, L.; Benelli, C.; Gatteschi, D. *Chem. Soc. Rev.* **2011**, *40*, 3092−3104.
(16) Hughes, I. D.; Dane, M.; Ernst, A.; Hergert, W.; Luders, M.; Poulter, J.; Staunton, J. B.; Svane, A.; Szotek, Z.; Temmerman, W. M. *Nature* **2007**, *446*, 650−653.
(17) Bunzli, J.-C. G.; Piguet, C. *Chem. Soc. Rev.* **2005**, *34*, 1048−1077.
(18) Bünzli, J.-C. G. *Chem. Rev.* **2010**, *110*, 2729−2755.
(19) Bünzli, J.-C. G.; Eliseeva, S. V. *Chem. Sci.* **2013**, *4*, 1939−1949.

(20) Roof, I. P.; Smith, M. D.; Cussen, E. J.; zur Loye, H.-C. *J. Solid State Chem.* **2009**, *182*, 295−300.
(21) Lin, J.; Diefenbach, K.; Cross, J. N.; Babo, J.-M.; Albrecht-Schmitt, T. E. *Inorg. Chem.* **2013**, *52*, 13278−13281.
(22) (a) Ok, K. M.; Zhang, L.; Halasyamani, P. S. *J. Solid State Chem.* **2003**, *175*, 264−271. (b) Sivakumar, T.; Ok, K. M.; Halasyamani, P. S. *Inorg. Chem.* **2006**, *45*, 3602−3605. (c) Lee, D. W.; Oh, S.-J.; Halasyamani, P. S.; Ok, K. M. *Inorg. Chem.* **2011**, *50*, 4473−4480. (d) Shen, Y.-L.; Mao, J.-G. *J. Alloys Compd.* **2004**, *385*, 86−89. (e) Shen, Y.-L.; Jiang, H.-L.; Xu, J.; Mao, J.-G.; Cheah, K. W. *Inorg. Chem.* **2005**, *44*, 9314−9321. (f) Shen, Y.-L.; Mao, J.-G. *Inorg. Chem.* **2005**, *44*, 5328−5335. (g) Jiang, H.-L.; Ma, E.; Mao, J.-G. *Inorg. Chem.* **2007**, *46*, 7012−7023. (h) Kong, F.; Jiang, H.-L.; Mao, J.-G. *J. Solid State Chem.* **2008**, *181*, 263−268. (i) Li, P.-X.; Zhang, S.-Y.; Mao, J.-G. *Dalton Trans.* **2010**, *39*, 11560−11567. (j) Sun, C.-F.; Hu, T.; Xu, X.; Mao, J.-G. *Dalton Trans.* **2010**, *39*, 7960−7967. (k) Henderson, N. L.; Baek, J.; Halasyamani, P. S.; Schaak, R. E. *Chem. Mater.* **2007**, *19*, 6058. (l) Retuerto, M.; Li, M. R.; Ignatov, A.; Croft, M.; Ramanujachary, K. V.; Chi, S.; Hodges, J. P.; Dachraoui, W.; Hadermann, J.; Tran, T. T.; Halasyamani, P. S.; Grams, C. P.; Hemberger, J.; Greenblatt, M. *Inorg. Chem.* **2013**, *52*, 12482−12491.
(23) (a) Mao, J.-G.; Jiang, H.-L.; Kong, F. *Inorg. Chem.* **2008**, *47*, 8498−8510. (b) Ok, K. M.; Halasyamani, P. S. *Chem. Mater.* **2001**, *13*, 4278−4284. (c) Goodey, J.; Broussard, J.; Halasyamani, P. S. *Chem. Mater.* **2002**, *14*, 3174−3180. (d) Ok, K. M.; Halasyamani, P. S. *Inorg. Chem.* **2002**, *41*, 3805−3807. (e) Goodey, J.; Ok, K. M.; Broussard, J.; Hofmann, C.; Escobedo, F. V.; Halasyamani, P. S. *J. Solid State Chem.* **2003**, *175*, 3−12. (f) Ok, K. M.; Halasyamani, P. S. *Inorg. Chem.* **2004**, *43*, 4248−4253. (g) Yu, R.; Min Ok, K.; Shiv Halasyamani, P. *Dalton Trans.* **2004**, 392−396. (h) Kim, J.-H.; Baek, J.; Halasyamani, P. S. *Chem. Mater.* **2007**, *19*, 5637−5641. (i) Frau, A. F.; Kim, J.-H.; Shiv Halasyamani, P. *Solid State Sci.* **2008**, *10*, 1263−1268. (j) Kim, J.-H.; Halasyamani, P. S. *J. Solid State Chem.* **2008**, *181*, 2108−2112. (k) Kim, M. K.; Kim, S.-H.; Chang, H.-Y.; Halasyamani, P. S.; Ok, K. M. *Inorg. Chem.* **2010**, *49*, 7028−7034. (l) Zhu, T.; Qin, J.; Halasyamani, P. S. *Dalton Trans.* **2011**, *40*, 8527−8532.
(24) (a) Hoss, P.; Starkulla, G.; Schleid, T. *Acta Crystallogr., Sect. E* **2005**, *61*, i113−i115. (b) Höss, P.; Osvet, A.; Meister, F.; Batentschuk, M.; Winnacker, A.; Schleid, T. *J. Solid State Chem.* **2008**, *181*, 2783−2788. (c) Meier, S. F.; Schleid, T. *J. Solid State Chem.* **2002**, *171*, 408−411. (d) Meier, S. F.; Hoss, P.; Schleid, T. *Z. Anorg. Allg. Chem.* **2009**, *635*, 768−775. (e) Meier, S. F.; Weber, F. A.; Gläser, R. J.; Schleid, T. *Z. Anorg. Allg. Chem.* **2001**, *627*, 2448−2450. (f) Weber, F. A.; Meier, S. F.; Schleid, T. *Z. Anorg. Allg. Chem.* **2001**, *627*, 2225−2231. (g) Weber, F. A.; Schleid, T. *Z. Anorg. Allg. Chem.* **2000**, *626*, 1285−1287. (h) Meier, S. F.; Schleid, T. *Z. Naturforsch., B: J. Chem. Sci.* **2004**, *59*, 881−888. (i) Meier, S. F.; Schleid, T. *Z. Naturforsch., B: J. Chem. Sci.* **2005**, *60*, 720−726.
(25) (a) *SADABS*; *TWINABS*; Bruker: Madison, WI, 2001. (b) *SAINT*; Bruker: Madison, WI, 2007.
(26) Bain, G. A.; Berry, J. F. *J. Chem. Educ.* **2008**, *85*, 532.
(27) Brese, N. E.; O'Keeffe, M. *Acta Crystallogr. Sect. B* **1991**, *47*, 192−197.
(28) (a) Volkringer, C.; Henry, N.; Grandjean, S.; Loiseau, T. *J. Am. Chem. Soc.* **2012**, *134*, 1275−1283. (b) Jin, G. B.; Skanthakumar, S.; Soderholm, L. *Inorg. Chem.* **2012**, *51*, 3220−3230. (c) Ling, J.; Ward, M.; Burns, P. C. *J. Solid State Chem.* **2011**, *184*, 401−404. (d) Daly, S. R.; Girolami, G. S. *Inorg. Chem.* **2010**, *49*, 4578−4585. (e) Salvadó, M. A.; Pertierra, P.; Castro, G. R.; Trobajo, C.; García, J. R. *Inorg. Chem.* **2008**, *47*, 1246−1248. (f) Forbes, T. Z.; Burns, P. C. *J. Solid State Chem.* **2007**, *180*, 106−112. (g) Forbes, T. Z.; Burns, P. C. *J. Solid State Chem.* **2005**, *178*, 3445−3452.
(29) *Lanthanide/Actinide Chemistry*; American Chemical Society: Washington, DC, 1967.
(30) Raymond, K. N.; Wellman, D. L.; Sgarlata, C.; Hill, A. P. *C. R. Chim.* **2010**, *13*, 849−852.
(31) Shannon, R. *Acta Crystallogr. Sect. A: Found. Crystallogr.* **1976**, *32*, 751−767.
(32) Kirby, A. F.; Foster, D.; Richardson, F. S. *Chem. Phys. Lett.* **1983**, *95*, 507−512.
(33) Xia, J.; Zhao, B.; Wang, H.-S.; Shi, W.; Ma, Y.; Song, H.-B.; Cheng, P.; Liao, D.-Z.; Yan, S.-P. *Inorg. Chem.* **2007**, *46*, 3450−3458.
(34) (a) Binnemans, K.; Görller-Walrand, C. *Chem. Phys. Lett.* **1995**, *235*, 163−174. (b) Carnall, W. T.; Fields, P. R.; Rajnak, K. *J. Chem. Phys.* **1968**, *49*, 4450−4455. (c) Carnall, W. T.; Fields, P. R.; Rajnak, K. *J. Chem. Phys.* **1968**, *49*, 4447−4449. (d) Carnall, W. T.; Fields, P. R.; Rajnak, K. *J. Chem. Phys.* **1968**, *49*, 4412−4423. (e) Carnall, W. T.; Fields, P. R.; Rajnak, K. *J. Chem. Phys.* **1968**, *49*, 4424−4442.